Quantitative Analysis of Soil Bearing Capacity Using Image-Based Morphology and Capacitive Moisture Sensing

Febry Mandasari, Eri Prasetyo Wibowo, Tubagus Maulana Kusuma, Sri Wulandari
[1]Department Information Technology, Gunadarma University, Depok, Indonesia,
[2]Department Civil Engineering, Gunadarma University, Depok, Indonesia
E-mail: febry_mandasari@staff.gunadarma.ac.id, eri@staff.gunadarma.ac.id, mkusuma@staff.gunadarma.ac.id, sri_wulandari@staff.gunadarma.ac.id

Keywords: soil morphology, image segmentation, Otsu thresholding, porosity index, dielectric capacitance, soil moisture sensor, pedon-scale, geotechnical screening

Received: January 5, 2026

This study proposes a rapid Pedon-scale screening framework for in-situ soil bearing capacity by integrating image-based soil morphology and capacitive moisture sensing. Six disturbed soil samples were collected from KIPP IKN (Nusantara), Mandalika (Central Lombok), Pulau Seram (Central Maluku), Desa Mayang (Sukoharjo), Penajam Paser Utara, and Ciracas (East Jakarta). Morphological structure was quantified from smartphone images acquired under controlled back-illumination using grayscale conversion, adaptive histogram equalization, Otsu thresholding, and morphological opening to obtain an image-derived porosity index treated as a void-ratio proxy. Moisture content was measured using a low-cost capacitive probe and mapped to percentage water content. Laboratory references followed ASTM standards (e.g., ASTM D2216 and D854) to compute gravimetric water content and void ratio. Agreement between rapid estimators and laboratory values was assessed using RMSE/NRMSE, normality testing, and Pearson correlation. The capacitive sensor achieved RMSE = 2.4366% (NRMSE = 7.56%) with r = 0.9956, while the image-based void-ratio proxy achieved RMSE = 0.0255 (NRMSE = 18.89%) with r = 0.8670. A rule-based fusion of porosity–moisture classes aligned fully with geotechnical bearing-capacity classification across sites. The proposed workflow offers a portable, low-cost alternative for rapid preliminary subgrade and foundation screening, while acknowledging uncertainty sources (illumination variability, heterogeneity, and sensor drift) for future field-scale validation.

Povzetek: Študija predstavlja hitro in cenovno ugodno metodo za oceno nosilnosti tal z uporabo slikovne analize in senzorja vlage, ki daje rezultate primerljive z laboratorijskimi meritvami, ob določenih omejitvah.

1 Introduction

Soil bearing capacity and subgrade performance are highly sensitive to moisture state; changes in water content (and matric suction) can significantly alter CBR and stiffness of compacted soils, affecting pavement/foundation decisions [1]. The water phase in soil is dynamic and significantly influences its mechanical properties, including shear strength, stiffness, and deformation response, which are essential for the stability of roads, foundations, and embankments [2]. Climate variability, such as extreme rainfall, prolonged droughts, and groundwater fluctuations, induces rapid changes in near-surface soil moisture, affecting soil features like crack development, pore connectivity, and surface roughness. Traditional measurement methods, such as gravimetric moisture content and point-based sensors, often fail to capture the heterogeneity of the soil and are limited in their spatial coverage. The increasing use of low-cost capacitive soil moisture sensors and IoT-based monitoring systems is promising, but these tools often overlook the complex interactions between the solid, liquid, and gas phases in the soil, leading to uncertainties in assessing the mechanical behavior and associated risks. This highlights the need for more integrated and informative approaches, such as using the three-phase soil model in combination with advanced data-driven techniques, to improve geotechnical assessments and enhance infrastructure resilience against fluctuating soil moisture conditions.

Soil morphology, encompassing pore characteristics, aggregates, cracks, and visual texture, constitutes a fundamental component of soil science as it underpins soil identification, classification, correlation, mapping, and interpretation across diverse land use contexts [3]. Traditionally, soil morphological characterization is conducted through direct field observation of soil profiles (Pedons) using standardized terminology and simple tools, including assessments of colour (Munsell scale), texture, structure, consistency, root and pore distribution, and horizon-specific features. Although these terminological frameworks have been progressively standardized over recent decades, soil morphology description remains largely qualitative and strongly dependent on the observer's expertise, which limits objectivity, reproducibility, and comparability across sites, observers, and temporal scales. As a result, conventional morphological descriptions provide limited quantitative

representation of soil structural features, such as pore systems, aggregate geometry, fracture patterns, and surface texture variability, which are increasingly required for data-driven land management, geotechnical analysis, and soil monitoring applications.

Classical soil morphology has long served as a fundamental basis for soil identification, classification, correlation, mapping, and interpretation within international soil taxonomy systems [4]–[6]. Standardized morphological descriptors such as colour, texture, structure, consistency, pores, roots, and horizon characteristics are widely applied to infer paedogenic processes influenced by parent material, climate, topography, organisms, and time [7]–[14]. Technological developments such as step-frequency ground penetrating radar and deep learning-based methods have begun to support soil morphological characterization and image-based classification [15], [16]. However, despite these advances, current soil morphology practices remain largely dominated by qualitative profile descriptions, with limited systematic quantification of pore, aggregate, and crack parameters derived from digital image analysis, and minimal linkage to in-situ sensor-based measurements

Research on capacitive moisture sensing demonstrates that variations in capacitance induced by changes in dielectric properties are widely exploited to measure moisture content in soil, air, and various engineering materials, owing to their high sensitivity, low cost, and compatibility with modern electronic systems [17]–[19]. In soil applications, numerous studies have reported that capacitive sensor responses are strongly influenced by salinity, soil type, and environmental conditions, thereby requiring careful calibration strategies and modelling of the soil–sensor interface to minimize measurement bias [20], [21]. Beyond geotechnical contexts, capacitive sensing techniques have been extensively applied in humidity sensors based on functional materials such as PEDOT:PSS, graphene oxide, cellulose, and porous dielectrics, including flexible and wireless systems for monitoring skin moisture, hydration status, and ambient environment [22]–[28]. Furthermore, the use of in-line capacitive sensors in polymer processing and fringing-field capacitive sensors in packaged food monitoring highlights the versatility of this technology for non-invasive moisture detection in industrial applications [17], [29]. Recent developments in battery-free RFID-based sensors and low-power wireless platforms have further expanded the feasibility of long-term and distributed moisture monitoring systems [30], [31], Nevertheless, existing studies predominantly emphasize sensor performance, signal stability, and calibration accuracy, while the influence of soil structural and morphological characteristics on capacitive sensor responses has received comparatively limited attention.
Similar integration efforts are also found in computer vision-based detection of moisture marks in underground infrastructures and in upscaling approaches that combine point-based moisture measurements with satellite observations. While these studies demonstrate the potential of combining imagery and moisture-related data across different application domains and spatial scales, their direct applicability to soil condition characterization at the Pedon-scale remains limited. Despite these advances, the quantitative linkage between soil morphological characteristics derived from images and in-situ capacitive moisture sensor responses at the Pedon-scale remains insufficiently explored.

In parallel fields such as autonomous robotics and nonlinear control, reliable state inference under real-world uncertainty is often achieved by fusing heterogeneous measurements with robust/adaptive estimation schemes [32]–[35]. Motivated by these developments, this study proposes an integrated workflow that combines image-based soil morphological analysis with capacitive moisture sensing to enable rapid soil-condition screening at the pedon-scale. In contrast to most prior studies that treat morphology and moisture sensing independently or operate at micro-scale laboratory imaging and macro-scale remote sensing, the proposed framework explicitly links a morphology-derived structural indicator an image-derived 2D porosity index as a proxy for void ratio with dielectric-based sensor response in a single, portable, and reproducible pipeline. The novelty therefore lies in the integration and Pedon-scale application of established techniques for practical, laboratory-benchmarked geotechnical screening, while recognizing that field deployment requires explicit attention to uncertainty sources such as lighting variability, soil heterogeneity, and sensor drift.

1.1 Research gap

Classical soil morphology studies have established a strong foundation for soil profile description and classification, however, they remain largely qualitative and lack systematic quantification of pore, aggregate, fracture, and visual texture parameters derived from image-based analysis. In parallel, research on soil moisture and capacitive sensing has primarily focused on sensor development, calibration strategies, and integration with wireless or remote sensing platforms, often treating soil as a homogeneous medium without explicit consideration of structural and morphological variability at the Pedon-scale. Existing attempts to integrate imagery and moisture sensing are predominantly applied to artificial structures or conducted at remote sensing scales, and do not explicitly link image-derived soil morphological indices with in-situ capacitive moisture sensor responses. Consequently, a clear scientific gap persists in the absence of an integrated framework capable of quantitatively mapping the relationship between image-based soil morphology/structure and capacitive moisture signals for rapid in-situ soil condition identification.

1.2. Research objectives

In line with the identified research gap, this study aims to develop and validate an integrated framework that combines image-based soil morphological analysis with capacitive sensor-based soil moisture measurements at the Pedon-scale for rapid in-situ soil condition identification. Specifically, the objectives of this study are to:

1. derive quantitative soil morphological indices from soil surface and profile images, encompassing pore characteristics, aggregate geometry, crack patterns, and visual texture attributes, using standardized image processing techniques;
2. evaluate statistical relationships and/or develop predictive models linking image-derived morphological indices with capacitive soil moisture sensor responses under varying soil types and moisture conditions; and
3. formulate and demonstrate a prototype scheme for rapid in-situ soil condition classification (e.g., moisture classes and/or structural condition categories) based on the combined use of image features and sensor signals.

Based on the identified research gap, this study is premised on the hypothesis that soil morphological and structural characteristics manifested through pore systems, aggregate geometry, crack patterns, and surface texture features are systematically reflected in the dielectric responses measured by capacitive soil moisture sensors at the Pedon-scale. Accordingly, image-based soil morphological information is expected to provide quantitative structural context that enhances the interpretation and calibration of capacitive sensor signals beyond conventional approaches that treat soil as a homogeneous medium. It is further anticipated that integrating image-derived morphological indices with capacitive moisture measurements will improve the accuracy of soil moisture estimation and enable more robust in-situ soil condition classification across varying soil types and moisture conditions.

These objectives are formulated to address RQ1–RQ3 by (1.) quantifying morphology-derived structure, (2.) validating capacitive moisture sensing, and (3.) demonstrating an integrated rule-based screening scheme for bearing-capacity classification.

1.3 Research questions

1. To what extent can an image-derived porosity index (void-ratio proxy) estimated via Otsu-based segmentation approximate laboratory void ratio/porosity values under controlled imaging conditions?

2. How accurately can a low-cost capacitive sensor estimate soil water content across different soil samples when validated against ASTM-based gravimetric measurements?

3. Does fusing morphology-derived structure (porosity proxy) and capacitive moisture measurements enable consistent Pedon-scale bearing-capacity classification comparable to geotechnical criteria used in practice?

2 Literature review

2.1 Digital image processing in soil digital image processing (DIP)

Digital Image Processing (DIP) in soil studies refers to a computer-based visual analysis approach that utilizes digital images to characterize soil properties such as morphology, texture, grain size distribution, particle shape, and soil type classification. Through a sequence of image acquisition, transformation, segmentation, feature extraction, and statistical analysis, DIP enables the quantitative characterization of soil microstructural features that are difficult to assess using conventional visual inspection methods [36], [37]. Based on its application and methodological focus, DIP in soil analysis can be categorized into several approaches. First, remote sensing-based DIP is widely used for large-scale soil mapping and land surface characterization using satellite or aerial imagery [38], Second, object-based and close-range image analysis focuses on soil classification and morphological characterization using laboratory or field-scale images, enabling more detailed assessment of soil structure and particle geometry [39], [40]. Third, the integration of DIP with machine learning algorithms, such as supervised classification and pattern recognition models, has enhanced the robustness and accuracy of soil interpretation under heterogeneous and uncontrolled field conditions [41], [42]. These developments demonstrate that DIP provides a fast, repeatable, and objective framework for soil characterization, with increasing relevance in geotechnical, agricultural, and environmental applications.

2.2 Capacitive moisture sensing

Capacitive moisture sensing is a widely used technique for estimating moisture content based on changes in the dielectric constant of a medium induced by variations in water content. As water has a significantly higher dielectric constant than air and soil minerals, changes in capacitance measured by the sensor can be directly related to moisture content, enabling real-time and non-destructive monitoring [19], [21]. From a conceptual perspective, capacitive moisture sensing can be categorized according to both sensor configuration and application context. In soil applications, capacitive sensors are commonly deployed as in-situ point sensors, requiring calibration to account for influencing factors such as soil texture, salinity, temperature, and bulk density, which can affect measurement accuracy [20]. Advances in electronics have further enabled the development of portable, low-cost, and IoT-based capacitive sensing systems, facilitating continuous soil moisture monitoring for irrigation management and land-use planning [30]. Beyond soil environments, capacitive moisture sensors have been adapted into flexible and wireless platforms for applications in medicine, industrial processing, and non-intrusive moisture monitoring in food packaging systems [24], [29]. These categorizations highlight the versatility of capacitive sensing technology,

while also emphasizing the importance of contextual calibration and interpretation when applied to heterogeneous soil media.

2.3 The integration of image morphology

The integration of image-based soil morphology analysis and moisture sensing represents an emerging approach for in-situ soil condition assessment, combining structural information derived from images with quantitative moisture measurements. Image-based analysis enables the extraction of morphological features such as pore distribution, aggregate structure, crack patterns, and surface texture, which are closely related to soil mechanical behavior, permeability, and hydraulic response [36], [37]. parallel, capacitive moisture sensors provide continuous estimates of water content, contributing to the assessment of soil consistency, degree of saturation, and bearing capacity. Existing studies on integration can be categorized based on application domain and spatial scale. Some approaches employ computer vision techniques for moisture detection and damage identification in artificial materials such as concrete and transportation infrastructure [43], Other studies adopt multi-scale or data fusion strategies, combining point-based moisture measurements with satellite-derived information to improve spatial soil moisture estimation [44]. While these studies demonstrate the feasibility of combining image-based analysis with moisture-related data, they are generally implemented in non-soil materials or at spatial scales that do not directly represent soil structure at the Pedon level. As a result, the methodological integration of quantitative soil morphological parameters with in-situ moisture sensor responses remains an active area of investigation within soil and geotechnical research.

Table 1: Previous research

No	Study (Year)	Task & Scale	Method	Dataset/Scenario	Key Result (reported metric)	Limitation / Gap vs this work
1	Velmurugan & Carlos (2009) [38]	Soil resource assessment & mapping (macro / regional)	Remote sensing + GIS + DIP	Satellite/remote sensing mapping context	Not explicitly reported in this manuscript	Operates at macro-scale; does not quantify pedon-scale morphology (pores/void proxy); no linkage with in-situ moisture sensing or bearing-capacity screening
2	Babalola et al. (2023) [41]	Soil surface texture classification (field images; close-range)	RGB imaging + deep learning/CNN	Uncontrolled field illumination conditions	Reported high accuracy for texture classification (specific metrics not stated here)	Focus on classification; not integrated with moisture sensing; no void ratio/porosity proxy; no geotechnical bearing-capacity interpretation
3	Kim et al. (2018) [40]	Particle/shape analysis linked to settling velocity (lab / micro-to-meso)	Digital image processing + geometry features	Particle images / laboratory setting	Not explicitly reported in this manuscript	Targets particle-scale settling; does not address pedon-scale pore structure; no integration with dielectric/capacitive moisture response
4	Alsultan et al. (2025) [30]	Long-term soil moisture monitoring (field/IoT context)	Battery-less UHF RFID capacitive sensor	Wireless, battery-free deployment scenario	Not explicitly reported in this manuscript	Emphasizes monitoring platform; does not link readings to morphology/void proxy; no integrated pedon-scale soil structure–moisture inference
5	Dawood et al. (2018) [43]	Moisture mark detection on concrete/subway infrastructure (non-soil material)	Computer vision + ML/DIP	Underground infrastructure surfaces	Not explicitly reported in this manuscript	Not applied to soils; no pedon-scale soil structure interpretation; no coupling between pore morphology and moisture sensor response
6	Greifeneder et al. (2016) [44]	Upscaling soil moisture from point to pixel (macro / remote sensing)	Multiscale data fusion (in-situ + satellite)	Point measurements + satellite pixels	Not explicitly reported in this manuscript	Focus on spatial upscaling; lacks pore/morphology imaging; does not relate microstructural indicators to sensor response; not aimed at rapid on-site bearing-capacity screening

3 Method

This study employs an integrated experimental–computational design to obtain rapid estimates of soil void ratio and water content and to validate these estimates against conventional laboratory measurements. The unit of analysis is disturbed soil specimens taken from the subsurface layer, for which both physical index properties and microstructural characteristics are quantified. The methodological framework consists of three main components standard geotechnical laboratory characterization, image-based porosity extraction, and capacitive sensor–based soil moisture measurement whose overall workflow is summarized in Figure 1. This integrated design is adopted to enable a direct, quantitative comparison between “ground truth” values obtained from ASTM-based testing and those derived from digital image analysis and low-cost sensi.

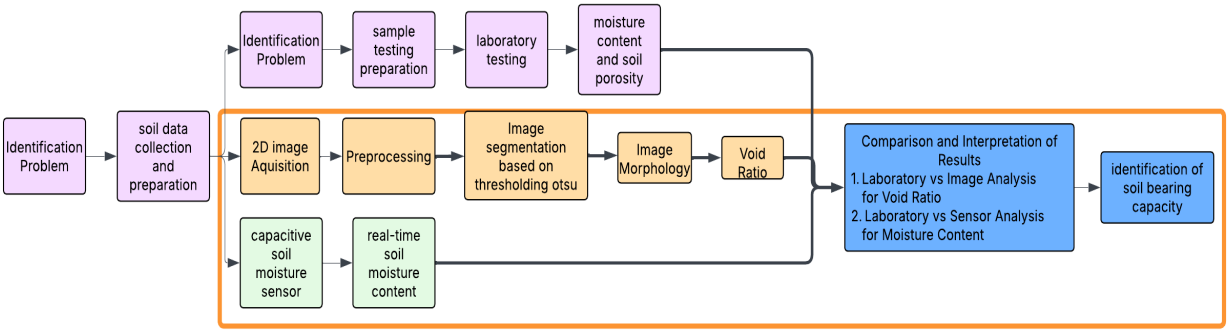

Figure 1: Research method

The research follows a quantitative, laboratory-based experimental design supported by computational image processing and basic statistical modelling. A purely numerical or simulation-based approach was deliberately avoided because the main objective of the study is to test whether digital and sensor-based estimators can approximate reference measurements obtained under controlled laboratory conditions. By combining physical testing, imaging, and electronic sensing within a single framework, the chosen design allows: (i) controlled manipulation of sample conditions (moisture and structure), (ii) replication of measurements across methods, and (iii) evaluation of error metrics between conventional and rapid-estimation techniques. This design is therefore appropriate for assessing the feasibility of rapid *in-situ* identification tools before field deployment.

Primary data are derived from soil sampling and laboratory testing, complemented by digital images and sensor readings acquired on the same materials. Soil samples were collected from depths of 50–100 cm to represent subsurface conditions that are less affected by short-term surface moisture fluctuations. The samples were sealed in airtight containers and transported to the Soil Mechanics Laboratory of Gunadarma University. Laboratory characterization followed relevant ASTM standards, including oven-drying at 105 °C for 24 hours for natural water content (ASTM D2216), pycnometer-based determination of specific gravity of soil solids (ASTM D854), bulk density and derived index properties using ring samplers (adapted from ASTM C29), and mechanical sieve analysis for grain-size distribution (ASTM D1140). A concise summary of parameters, methods, and standards is presented in Table 1. Water content was computed as

$$w = \frac{W_w}{W_s} \times 100\%,$$

void ratio as

$$e = \frac{V_v}{V_s}, \qquad n = \frac{e}{1+e},$$

and grain-size descriptors as

$$C_u = \frac{D_{60}}{D_{10}}, \qquad C_c = \frac{D_{30}^2}{D_{10}D_{60}}.$$

These formulations provide the quantitative baseline against which image and sensor-based estimations are evaluated.

Data collection for the computational components consisted of two parallel streams: (1) image acquisition for porosity/void-ratio proxy estimation and (2) electronic measurement for soil moisture. For the imaging stream, approximately 40 g of wet soil was placed in a 10 cm glass petri dish and illuminated from below using an LED panel inside a dark enclosure to ensure uniform, glare-free lighting. A 50 MP smartphone camera, positioned 3–5 cm above the sample, captured high-resolution 2D images of the soil surface. The image-processing pipeline comprised: (i) RGB-to-grayscale conversion, (ii) contrast enhancement using adaptive histogram equalization, (iii) segmentation using Otsu's global thresholding to separate pore and solid regions, and (iv) morphological opening to suppress small artifacts and smooth boundaries. Otsu thresholding was selected because the back-illumination setup tends to produce a bimodal grayscale distribution (transmissive pores vs. opaque soil matrix), enabling parameter-free and reproducible segmentation without manual tuning across samples. The complete workflow is illustrated in Figure 2.

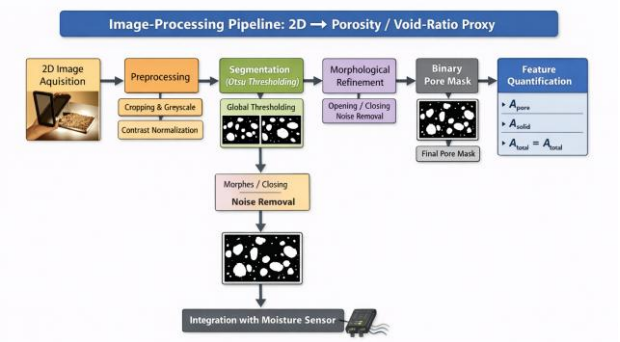

Figure 2: Image-processing pipeline

Following segmentation and morphological refinement, the resulting binary pore mask was used to compute an image-derived porosity index. This was also expressed as an image-based void-ratio proxy (e_img) by taking the ratio between the total area of connected pore regions and the total area of solid regions in the segmented image. This metric is treated as a proxy for relative

structural openness rather than a direct replacement of the 3D laboratory void ratio.

In parallel, soil water content was measured using a capacitive soil moisture sensor to obtain rapid, non-destructive readings. The sensor detects changes in the bulk dielectric response of the soil, producing raw outputs ranging from 0 (very wet) to 615 (very dry), which were converted into moisture content using the calibration mapping adopted in this study.

Data analysis proceeds in three stages: physical parameter derivation, integration of porosity and moisture indicators, and statistical validation. First, laboratory measurements are used to compute reference values of water content, void ratio, porosity, and related index properties as described above. Second, image-derived porosity indices and sensor-derived moisture contents are jointly interpreted through a rule-based scheme that maps combinations of void ratio class (low, medium, high) and moisture class (low, medium, high) to qualitative descriptions of bearing capacity commonly used in geotechnical practice (e.g., "high bearing capacity", "reduced capacity", "very low capacity"). This step operationalizes the integrated use of structural and hydraulic indicators for rapid *in-situ* soil condition assessment. Third, the agreement between rapid-estimation methods and laboratory references is quantified using Root Mean Squared Error (RMSE) and Normalized RMSE (NRMSE), with

$$\mathrm{RMSE} = \sqrt{\frac{1}{N}\sum_{i=1}^{N}(y_i - \hat{y}_i)^2}, \mathrm{NRMSE} = \frac{\mathrm{RMSE}}{y_{\max} - y_{\min}} \times 100\%.$$

Kolmogorov–Smirnov tests are applied to check normality assumptions, and Pearson correlation coefficients are computed to evaluate the strength of linear relationships between laboratory-derived and model-derived values for both water content and porosity.

Pearson correlation was selected to assess linear association after verifying approximate normality using the Kolmogorov–Smirnov test ($p > 0.05$). RMSE and NRMSE were used as scale-sensitive and normalized error metrics for agreement assessment. All statistics were computed under the assumption that paired laboratory–estimator observations represent the same specimen condition, with no missing data.

3.1 Uncertainty sources and robustness measures

Although the proposed framework is primarily validated through laboratory benchmarking, several practical uncertainty sources relevant to field deployment were considered in the experimental design. For image-based porosity extraction, lighting variability was minimized by using a dark enclosure, fixed camera-to-sample distance, and back-illumination to reduce specular reflections; additionally, grayscale normalization and morphological opening were applied to reduce segmentation sensitivity to small artifacts and non-uniform intensity. For capacitive sensing, measurement repeatability was promoted by keeping probe insertion depth consistent and using the same acquisition protocol for all specimens, however, the authors acknowledge that capacitive readings may be affected by soil salinity, texture, temperature, and long-term sensor drift, which motivates calibration procedures and periodic re-referencing in extended deployments. From a systems perspective, these uncertainty sources resemble measurement noise, bias, and unmodelled dynamics in intelligent sensing and nonlinear control applications, where robust/adaptive estimation is often used to preserve reliability [42]–[46]. Therefore, while the present study focuses on establishing feasibility and laboratory agreement, the framework is designed to be compatible with future uncertainty-aware fusion (e.g., adaptive mapping of sensor signals conditioned on morphology-derived structural indicators) to improve robustness in real field conditions.

4 Result

This section presents the laboratory and computational results for six disturbed soil samples collected from KIPP IKN (Nusantara), Mandalika (Lombok Tengah), Pulau Seram (Maluku Tengah), Desa Mayang (Sukoharjo), Penajam Paser Utara (PPU), and Ciracas (East Jakarta). The analyses include basic index properties (water content and specific gravity), bulk density and void ratio, image-based pore characterization, in-situ moisture measurements using a capacitive soil moisture sensor, and statistical evaluation of agreement between laboratory and computational/sensor-based methods.

4.1.Basic index properties of the soils

4.1.1. Gravimetric water content

Gravimetric water content obtained from laboratory oven-drying tests varies substantially between locations. In Table 2, The highest water content is observed for KIPP IKN (43.42%), followed by Mandalika (40.79%), while the driest soil is from PPU (20.96%). Intermediate values occur at Pulau Seram (33.99%), Ciracas (28.76%), and Mayang (25.45%). These values indicate that IKN and Mandalika soils can be classified as high-water-content soils ($w > 40\%$), whereas PPU exhibits relatively low in-situ moisture under the tested condition.

Table 2: Laboratory water content of soils at six locations

Soil Sampling Location	Water Content, w (%)
KIPP IKN	43.42
Mandalika	40.79
Pulau Seram	33.99
Ciracas	28.76
Mayang	25.45
PPU	20.96

4.1.2. Specific gravity of soil solids

Specific gravity (Gs) values also differ between sites, reflecting variations in mineralogical composition. In Table 3, the highest Gs is recorded for Pulau Seram (2,820), consistent with the presence of heavier phyllosilicate minerals, whereas the lowest Gs values are found at Mandalika (2,383) and PPU (2,450). KIPP IKN (2,653) and Mayang (2,635) exhibit similar specific gravities, suggesting comparable feldspar- and mica-dominated assemblages, while Ciracas shows an intermediate value of 2,620.

Table 3: Specific gravity (Gs) of soil samples at six locations

Soil Sampling Location	Specific gravity (Gs)
Pulau Seram	2,820
KIPP IKN	2,653
Mayang	2,635
Ciracas	2,620
PPU	2,450
Mandalika	2,383

4.1.3. Bulk density and laboratory void ratio

Bulk density tests provide water content and void ratio values under controlled compaction in the laboratory rings. In Table 4, the void ratios (e) range between 0.10 and 0.21, with the highest e obtained for PPU (0.21) and the lowest for Ciracas (0.10). KIPP IKN and Mandalika soils show intermediate void ratios of 0.15 and 0.12, respectively, while Mayang and Pulau Seram both exhibit e ≈ 0.11–0.12. Overall, all samples fall into the category of low void ratio (e < 0.5), corresponding to relatively dense soils in laboratory conditions.

Table 4: Water content and void ratio from bulk density tests

Soil Sampling Location	Water Content, w (%)	Void Ratio
KIPP IKN	43.42	0.15
Mandalika	40.79	0.12
Pulau Seram	33.99	0.11
Ciracas	28.76	0.10
Mayang	25.45	0.12
PPU	20.96	0.21

4.2.Image-based pore characterization

Representative images for each soil sample include RGB images, gray-level conversions, binary images obtained using Otsu's thresholding, binary pore masks, and pore depth/brightness maps generated under back-lighting.

For Mandalika soil, Figure 3 presents the complete image-processing pipeline. In Figure 3, the original RGB image (Figure 3a) and the grayscale image (Figure 3b) show bright zones corresponding to relatively large and continuous pores, whereas dark zones represent the soil skeleton; the binary image (Figure 3c) clearly indicates that black pixels (solid) dominate over white pixels (pores). After morphological opening, the pore mask in Figure 1d yields a total pore area of approximately 1.53×10^6 pixel², compared with 1.10×10^7 pixel² for solids, resulting in an image-based void ratio e = 0.14. The pore-depth map in Figure 1e highlights only a few red (high-intensity) regions, indicating that highly transmissive pore channels are relatively rare.

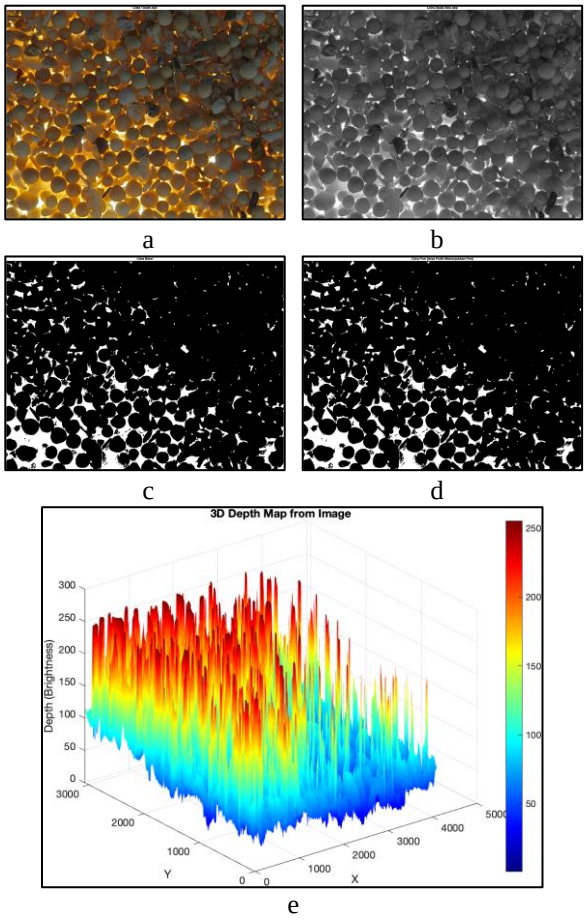

Figure 3: Image-processing pipeline for Mandalika soil (RGB, grayscale, binary, pore mask, and depth map)

For the KIPP IKN soil (Desa Girimukti), Figure 4 shows a similar processing sequence. In Figure 2, the RGB and grayscale panels (Figure 4a–b) contain fewer and more discontinuous bright zones than Figure 3, and the pore mask in Figure 4d displays smaller and more isolated clusters of white pixels, indicating a more compact microstructure. The total pore area is 1.39×10^6 pixel², slightly lower than in Mandalika, while the solid area is 1.12×10^7 pixel², resulting in an image-based void ratio e = 0.12. The depth map in Figure 4e contains fewer red zones and more green–blue tones, confirming that deep or strongly connected pores are less developed at KIPP IKN.

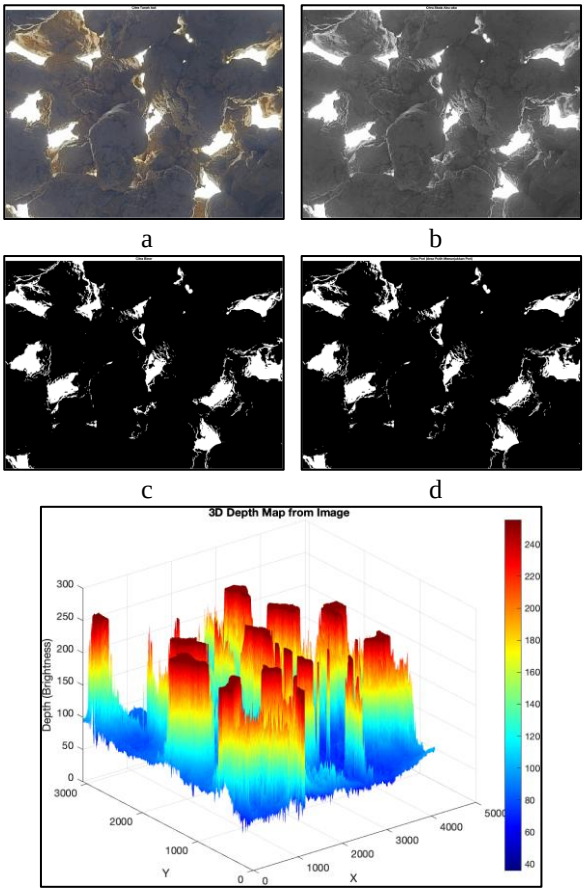

Figure 4: Image-processing pipeline for KIPP IKN soil

Pulau Seram soil displays a more heterogeneous pore distribution. In Figure 5, the RGB and binary images show irregularly distributed bright and pore regions, and the pore mask reveals a more scattered pattern of white pixels compared with Figures 3 and 4. The total pore area corresponds to an image-based void ratio of e ≈ 0.14, comparable to Mandalika, but the spatial distribution suggests that pores are less uniformly arranged. The depth map contains several medium-intensity regions, indicating moderate but not continuous light transmission.

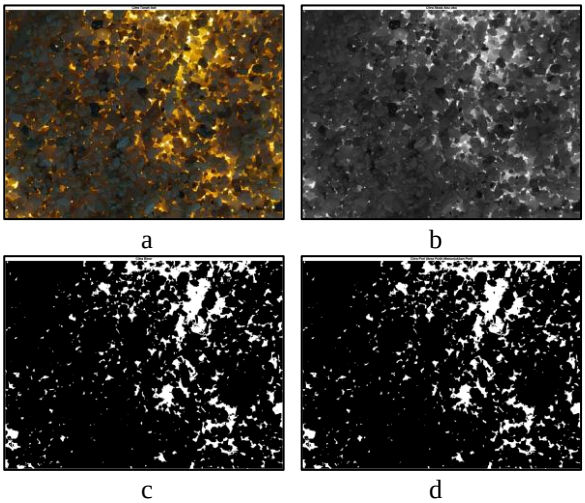

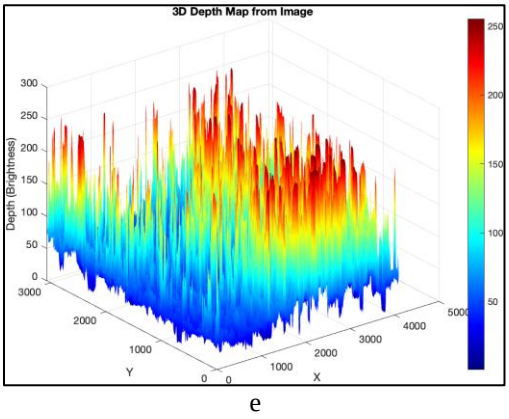

Figure 5: Image-processing pipeline for Pulau Seram soil.

Mayang soil appears visually denser than Mandalika and Pulau Seram. In Figure 6, the bright regions are limited and mostly confined to small spots, and the pore mask shows that white pore pixels occupy only a small fraction of the total area. The computed image-based void ratio is e ≈ 0.10. The depth map is dominated by blue and green tones, with very few yellow or red zones, implying that most pores are shallow or poorly connected. This visual pattern supports the interpretation that Mayang soil has a relatively high bearing capacity due to its dense structure.

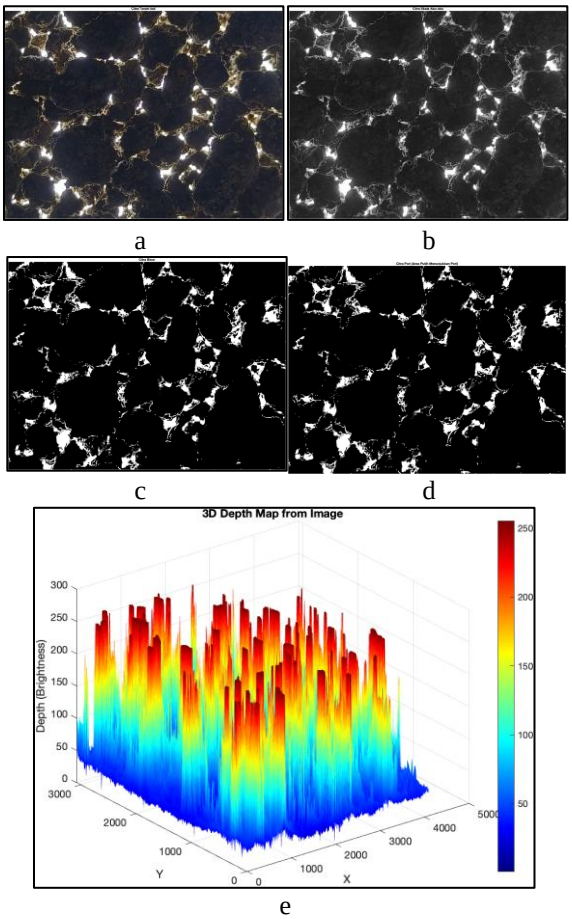

Figure 6: Image-processing pipeline for Mayang soil

PPU soil contrasts sharply with Mayang and Ciracas. In Figure 7, more extensive bright regions are observed in the RGB and grayscale images, and the pore mask contains a visibly larger proportion of white pixels, leading to the highest image-based void ratio among all locations (e = 0.23). The depth map includes several red and yellow zones, suggesting deep and well-connected pore channels that allow strong light transmission. Even though the laboratory void ratio remains low (e = 0.21), the figure clearly demonstrates a more open pore connectivity in PPU soil compared with the other samples.

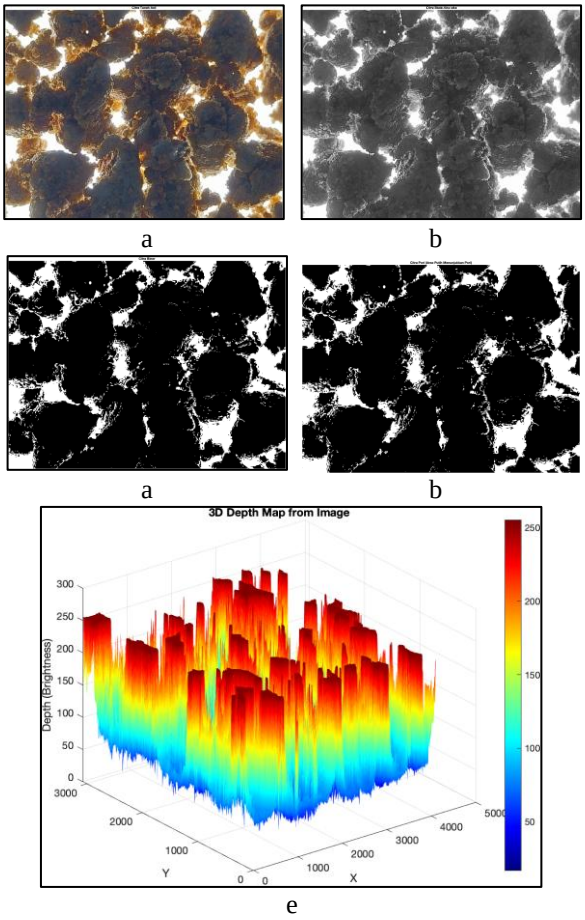

Figure 7: Image-processing pipeline for PPU soil.

Ciracas soil is the densest among the investigated locations. In Figure 8, bright regions are minimal and the specimen appears mostly dark in both RGB and grayscale forms, indicating a very limited pore network; the pore mask shows the smallest amount of white pixels, corresponding to an image-based void ratio of e = 0.07. The depth map is dominated by dark blue shades with almost no red or yellow zones, confirming that there are very few pores capable of transmitting light over significant depths. This evidence supports the classification of Ciracas soil as having a very dense microstructure and potentially high bearing capacity.

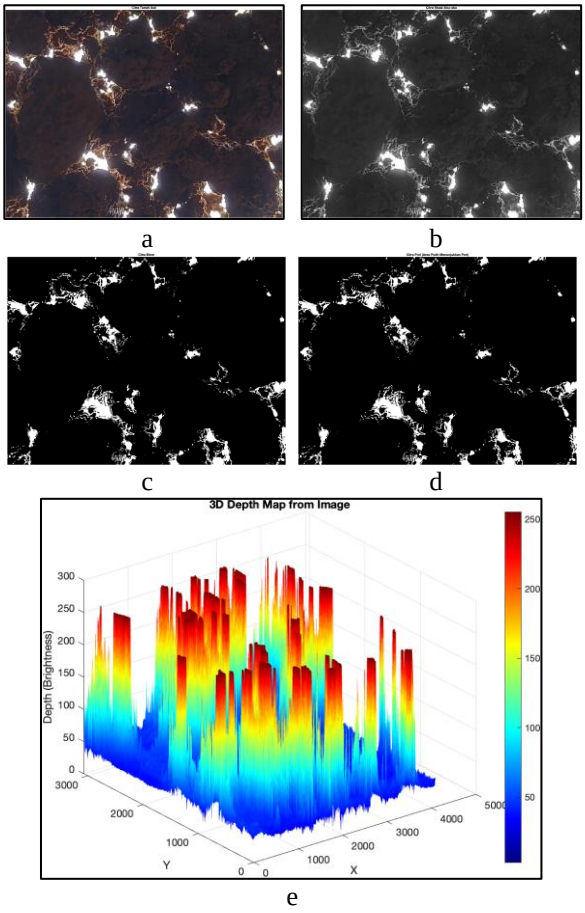

Figure 8: Image-processing pipeline for Ciracas soil.

Taken together, Figures 3–8 show that all soils fall in the low-void-ratio regime (e < 0.5), but with distinct differences in pore distribution and connectivity: Mandalika and Pulau Seram present moderate void ratios with heterogeneous pores, PPU has the largest and most connected pores, while Mayang and especially Ciracas show very limited pore networks consistent with dense packing.

4.3. In-situ water content from capacitive soil moisture sensor

Field water content was measured using a capacitive soil moisture sensor connected to an Arduino platform. In Table 5, the sensor-based water contents range from 20% to 47%, with the highest value at KIPP IKN (47%) and the second highest at Mandalika (44%), while the lowest value is recorded at PPU (20%). Intermediate values of 36%, 30%, and 23% are obtained for Pulau Seram, Ciracas, and Mayang, respectively. These sensor-based values are systematically higher but broadly consistent with gravimetric laboratory water contents, reflecting the fact that the sensor captures field moisture conditions, whereas the laboratory values are derived from controlled gravimetric measurements on disturbed samples.

Table 5: In-situ water content measured by capacitive soil moisture sensor.

Soil Sampling Location	Water Content, w (%)
KIPP IKN	47.00
Mandalika	44.00
Pulau Seram	36.00
Ciracas	30.00
Mayang	23.00
PPU	20.00

4.4. Comparison between laboratory and sensor-based water content

A direct comparison between gravimetric laboratory water contents and capacitive-sensor readings is summarized in Table 6 and graphically illustrated in Figure 9. Across all sampling locations, the relative ranking of water content is preserved by both methods: KIPP IKN and Mandalika remain the wettest sites, whereas PPU is consistently the driest. The absolute differences between laboratory and sensor values range from 0.96% (PPU) to 3.58% (KIPP IKN), which are small compared with the total water content. This consistency indicates that the capacitive soil moisture sensor provides a reasonably accurate proxy for laboratory-determined water content across the tested soil types.

Table 6: Absolute differences between laboratory and capacitive-sensor water contents.

Soil Sampling Location	Water Content, w (%)		Absolute Difference
	Laboratory	Capacitive Soil Moisture Sensor	
KIPP IKN	43.42	47.00	3.58
Mandalika	40.79	44.00	3.21
Pulau Seram	33.99	36.00	2.01
Ciracas	28.76	30.00	1.24
Mayang	25.45	23.00	2.45
PPU	20.96	20.00	0.96

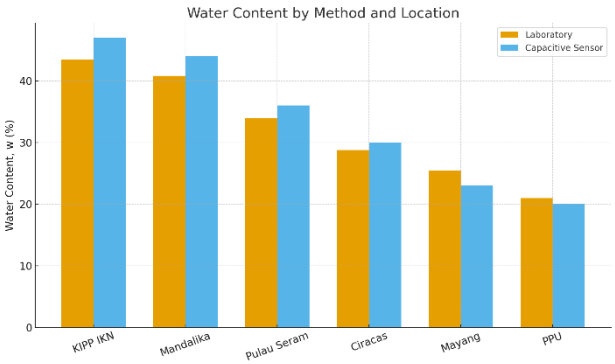

Figure 9: Water content obtained from laboratory and capacitive soil moisture sensor at each sampling location.

4.5. Comparison between laboratory and image-based void ratio

Void ratios obtained from bulk-density tests (laboratory e) and from image-morphology analysis (image e) are summarized in Table 7 and plotted in Figure 10. For all sampling locations, both methods yield low void ratios ($e < 0.5$), with the largest values occurring at PPU ($e_{lab} = 0.21$, $e_{img} = 0.23$) and the smallest at Ciracas ($e_{lab} = 0.10$, $e_{img} = 0.07$). Across sites, the differences between laboratory and image-based values are small, typically on the order of 0.02–0.03. These results indicate that image-based morphology analysis can reproduce laboratory-derived void ratios with only minor deviations, even though the two approaches rely on different physical principles.

Table 7: Absolute differences between laboratory and image-based void ratios.

Soil Sampling Location	Void Ratio (*e*)		Absolute Difference
	Laboratory	*Image Morphology*	
KIPP IKN	0.15	0.12	0.03
Mandalika	0.12	0.14	0.02
Pulau Seram	0.11	0.14	0.03
Ciracas	0.10	0.07	0.03
Mayang	0.12	0.10	0.02
PPU	0.21	0.23	0.02

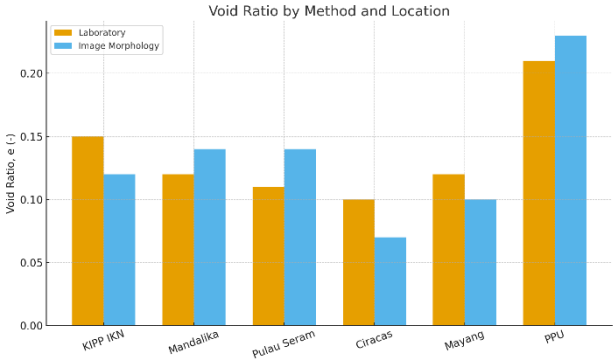

Figure 10: Void ratio obtained from laboratory testing and image-morphology analysis at each sampling location.

4.6. Error metrics and statistical validation

The agreement between laboratory and computational/sensor-based measurements was further quantified using Root Mean Squared Error (RMSE) and Normalized RMSE (NRMSE), as summarized in Table 8. In Table 9, the RMSE between laboratory and capacitive sensor water contents is 2.436%, with NRMSE = 7.56%, whereas the RMSE between laboratory and image-based void ratios is 0.0255, with NRMSE = 18.89%. These relatively small error values indicate good predictive capability of both the capacitive sensor for water content and the image morphology approach for void ratio.

Normality of the datasets was evaluated using the Kolmogorov–Smirnov test, and linear association was assessed with Pearson correlation; the results can be

reported in an additional summary table if required. In the normality analysis, the void ratio data yield h = 0 and p = 0.6223, while the water content data yield h = 0 and p = 0.9837, indicating that both sets are normally distributed (p > 0.05). The Pearson correlation coefficients show very strong linear relationships, with r = 0.8670 for laboratory versus image-based void ratios and r = 0.9956 for laboratory versus sensor-based water contents. These statistics confirm that the proposed computational and sensor-based methods capture the same trends as the laboratory tests with high fidelity.

Table 8: RMSE and NRMSE for water content and void ratio.

Accuracy Model	Laboratory Test with Capacitive Soil Moisture Sensor	Laboratory Test with Otsu Thresholding Based Image Segmentation
RMSE	2.436	0.0255
NRMSE	7.56 %	18.89%

5 Discussion

5.1 Interpretation of agreement with laboratory references

The results indicate that the proposed rapid estimators preserve the same ranking and trends produced by standard laboratory measurements across the six sites. The capacitive sensor exhibited a low NRMSE (7.56%) and near-perfect linear association (r = 0.9956) with gravimetric water content, while image-derived porosity/void ratio proxy achieved a small absolute deviation (typically 0.02–0.03) and a strong correlation (r = 0.8670). This suggests that morphology-derived pore indicators provide meaningful structural information that complements direct moisture sensing, enabling a consistent soil condition interpretation when mapped to geotechnical bearing-capacity criteria.

Compared with prior soil-image studies that primarily target texture/type classification or particle-shape characterization, the present work focuses on a geotechnical indicator pathway by translating image morphology into a porosity index used as a void-ratio proxy, and then fusing it with in-situ dielectric sensing to support bearing-capacity screening at the pedon-scale. Unlike sensor-centric studies that report calibration performance without structural context, the proposed framework explicitly incorporates morphology-derived structure to interpret moisture response and to enable rule-based capacity classification. The observed agreement with ASTM-referenced laboratory measurements (RMSE and strong correlations for both moisture and void-ratio proxy) indicates that the integration provides not only descriptive imaging or point moisture readings, but a practical decision-support layer for rapid screening.

5.2 Practical implications for rapid geotechnical screening

From an applied standpoint, the integrated morphology–moisture framework supports rapid decision-making scenarios such as preliminary subgrade assessment, construction screening, and early-stage foundation feasibility checks. The method is portable and computationally lightweight (smartphone imaging + low-cost capacitive probe), which makes it suitable for repeated measurements over short time windows to capture moisture-driven changes. This role is conceptually analogous to real-time monitoring and decision support in autonomous systems, where multiple data streams are fused to infer states needed for safe operation [33], [45].

5.3 Robustness considerations: lighting variability, heterogeneity, and sensor drift

Despite the strong laboratory agreement, real-world field conditions introduce uncertainty that is not explicitly modelled in the current formulation. First, illumination changes can affect threshold-based segmentation; although the enclosure and back-lighting reduce this sensitivity, uncontrolled sunlight, shadows, and surface wetness may still perturb grayscale distributions and binary pore masks. Second, soil heterogeneity at the pedon-scale (variable aggregation, mixed grain sizes, localized salinity) can cause the image-derived porosity proxy to differ from bulk void ratio and can also alter dielectric properties measured by capacitive sensors. Third, capacitive probes may exhibit drift and bias due to aging, temperature dependence, and soil–sensor interface effects, potentially degrading accuracy over time. In intelligent control and estimation, analogous issues are treated as disturbances, modelling uncertainty, and measurement noise, and robustness is improved through adaptive/robust schemes such as practical finite-time fuzzy sliding-mode designs that suppress chattering-like effects and maintain stability under uncertainty [46], as well as robust adaptive output-feedback controllers that compensate for unknown nonlinearities and time-varying dynamics using learning-based approximation and Lyapunov-type arguments [34]. By comparison, the current geotechnical framework uses deterministic feature extraction and direct calibration, which is adequate for feasibility demonstration but can be strengthened by incorporating explicit uncertainty handling for field deployment.

5.4 Limitations and future work

The present validation covers six disturbed samples and a limited range of moisture states, which constrains generalization across broader soil classes (e.g., expansive clays, highly organic soils, cemented lateritic soils) and environmental conditions. To increase scientific impact and practical relevance, future work should (i) expand the dataset across more soil types, gradations, salinity/temperature regimes, and controlled wetting–drying cycles, and (ii) evaluate repeatability under field-like illumination and probe insertion variability. In addition, the framework can be extended from rule-based mapping to uncertainty-aware fusion, for example by learning a moisture estimator conditioned on morphology-derived indices (porosity, crack density, aggregate

metrics) and applying adaptive updating to mitigate drift. Such an extension aligns with multi-source inference paradigms commonly used in robotics and nonlinear optimal control applications, where stability-preserving structures (e.g., successive-loop/flatness-based designs and nonlinear optimal control formulations) provide a pathway to robust operation under real-world perturbations [32], [33]. Ultimately, positioning the method as part of a smart/automated geotechnical assessment pipeline (image + probe + embedded analytics) could enable scalable, data-driven field screening that complements conventional laboratory testing.

Future validation will target a broader soil taxonomy (coarse-grained, fine-grained/high-plasticity, organic-rich, and lateritic soils) and multiple controlled moisture states per soil via wetting–drying cycles to quantify repeatability and generalization.

6 Conclusion

This study demonstrates that integrating 2D image-based morphological analysis with capacitive moisture sensing can provide fast and reasonably accurate estimates of soil condition indicators relevant to rapid field screening. The image-processing pipeline based on Otsu thresholding and morphological operations produced an image-derived porosity/void ratio proxy that was consistent with laboratory-based void ratio trends, while the capacitive sensor yielded moisture estimates with a low error relative to gravimetric measurements. Quantitative validation using RMSE and NRMSE confirmed a strong level of conformity between the proposed rapid estimators and conventional laboratory references. The main contribution of this work is an IT-based soil characterization framework that links morphology-related descriptors (e.g., pores and texture patterns) with real-time moisture response at the pedon-scale, supporting practical applications such as rapid geotechnical surveys, preliminary subgrade screening, construction monitoring, and land management.

Despite the promising agreement, the approach remains sensitive to real-world uncertainties. Image-based morphology may be affected by illumination changes and surface glare, while capacitive sensing may require additional calibration across soil types due to soil–sensor interface effects and potential drift. In addition, field deployment may introduce further uncertainty sources, including spatial heterogeneity at the pedon-scale, moisture-state dynamics, and long-term sensor drift that are not explicitly modelled in the present deterministic formulation. Future work will therefore expand validation to broader soil classes and controlled moisture trajectories (wetting–drying cycles), increase sampling density per site, and investigate uncertainty-aware, adaptive fusion strategies inspired by robust/adaptive estimation methods in nonlinear control to improve reliability under field conditions [32]–[34], [45], [46].

7 Acknowledgment

The authors gratefully acknowledge the Rector and Vice Rector II of Gunadarma University for their invaluable support, particularly for providing funding for the publication of this research. Their assistance and contribution have been instrumental in the completion of this work.

References

[1] S.-M. Lim *et al.*, “Influence of matric suction on resilient modulus and CBR of compacted Ballina clay,” *Constr. Build. Mater.*, vol. 359, p. 129482, 2022, doi: 10.1016/j.conbuildmat.2022.129482.

[2] L. H. Stolzy and W. A. Jury, “Soil physics,” in *Handbook of Soils and Climate in Agriculture*, 2018, pp. 131–158. doi: 10.1201/9781351073073.

[3] J. Bouma, “Soil morphology and preferential flow along macropores,” *Agric. Water Manag.*, vol. 3, no. 4, 1981, doi: 10.1016/0378-3774(81)90009-3.

[4] P. R. Owens and Z. Libohova, “Soil morphology,” in *Encyclopedia of Soils in the Environment, Second Edition*, 2023, pp. V4-149. doi: 10.1016/B978-0-12-822974-3.00142-7.

[5] D. Kühn and E. Eberhardt, “A classification of soil solid material for natural and anthropogenic soils,” *J. Plant Nutr. Soil Sci.*, vol. 186, no. 5, pp. 507–521, 2023, doi: 10.1002/jpln.202200444.

[6] D. Pietsch and B. Lucke, “Soil substrate classification and the FAO and World Reference Base systems: Examples from Yemen and Jordan,” *Eur. J. Soil Sci.*, vol. 59, no. 4, pp. 824–834, 2008, doi: 10.1111/j.1365-2389.2008.01017.x.

[7] J. C. Dixon, “Pedogenesis with Respect to Geomorphology,” in *Treatise on Geomorphology: Volume 1-14*, vol. 1–14, 2013, pp. 27–43. doi: 10.1016/B978-0-12-374739-6.00058-0.

[8] Y. Liu, X. Sun, L. Nie, and Y. Qiao, “Genetic characteristics and taxonomic classification of soils developed on Sygera Mountain of Tibet, China,” *Environ. Earth Sci.*, vol. 75, no. 2, pp. 1–9, 2016, doi: 10.1007/s12665-015-4893-6.

[9] N. I. Mansyur, E. Hanudin, B. H. Purwanto, and S. N. H. Utami, “Morphological characteristics and classification of soils formed from acidic sedimentary rocks in North Kalimantan,” in *IOP Conference Series: Earth and Environmental Science*, 2019, vol. 393, no. 1. doi: 10.1088/1755-1315/393/1/012083.

[10] L. McFadden, “Soil Morphology in Quaternary Studies,” in *Encyclopedia of Quaternary Science*, 2006, pp. 2126–2137. doi: 10.1016/B0-44-452747-8/00154-X.

[11] D. R. Muhs, “Soils and Paleosols,” in *Encyclopedia of Geology: Volume 1-6, Second Edition*, vol. 5, 2020, pp. 370–384. doi: 10.1016/B978-0-12-409548-9.12002-0.

[12] D. G. Polyakov, I. V Kovda, and A. G. Ryabukha, "Soils of Chalk Polygons of the Sub-Ural Plateau: Morphology, Properties, and Classification," *Eurasian Soil Sci.*, vol. 57, no. 1, pp. 176–188, 2024, doi: 10.1134/S1064229323602445.

[13] E. V Zhangurov, M. P. Lebedeva, and I. V Zaboeva, "Microstructure of genetic horizons in automorphic soils of the Timan Ridge," *Eurasian Soil Sci.*, vol. 44, no. 3, pp. 261–271, 2011, doi: 10.1134/S1064229311030203.

[14] S. V Gubin, "Cryogenic Impact on the Formation of Permafrost-Affected Loamy Tundra Soils at Different Stages of Development," *Eurasian Soil Sci.*, vol. 58, no. 3, 2025, doi: 10.1134/S1064229324601732.

[15] F. Lombardi and M. Lualdi, "Step-frequency ground penetrating radar for agricultural soil morphology characterisation," *Remote Sens.*, vol. 11, no. 9, 2019, doi: 10.3390/rs11091075.

[16] K. H. Rahouma and R. H. M. Aly, "Soil Morphology Based on Deep Learning, Polynomial Learning and Gabor Teager-Kaiser Energy Operators," in *Studies in Big Data*, vol. 77, 2021, pp. 325–346. doi: 10.1007/978-3-030-59338-4_17.

[17] D. Barrettino, G. Badaracco, M. Sala, F. Piffaretti, and M. Sammartini, "In-line capacitive moisture sensor for polymer industries," in *Conference Record - IEEE Instrumentation and Measurement Technology Conference*, 2013, pp. 581–586. doi: 10.1109/I2MTC.2013.6555483.

[18] A. Fuchs, H. Zangl, and G. Holler, "Capacitance-based sensing of material moisture in bulk solids: Applications and restrictions," in *Lecture Notes in Electrical Engineering*, 2008, vol. 20 LNEE, pp. 235–248. doi: 10.1007/978-3-540-79590-2_16.

[19] M. Tomar and T. Patidar, "Development of a low Cost Soil Moisture Sensor," in *Proceedings - International Conference on Vision Towards Emerging Trends in Communication and Networking, ViTECoN 2019*, 2019. doi: 10.1109/ViTECoN.2019.8899399.

[20] P. Johnson, K. Watling, D. V Thiel, and D. A. James, "Validation of a soil interface model to account for apparent aberrations in capacitive soil moisture sensors," in *Proceedings of SPIE - The International Society for Optical Engineering*, 2006, vol. 6035. doi: 10.1117/12.639118.

[21] S. Ahmad, N. Khalid, and R. Mirzavand, "Detection of Soil Moisture, Humidity, and Liquid Level Using CPW-Based Interdigital Capacitive Sensor," *IEEE Sens. J.*, vol. 22, no. 11, pp. 10338–10345, 2022, doi: 10.1109/JSEN.2022.3167337.

[22] J. Chen, F. Yu, Y. Wang, and D. Ke, "Theoretical model for a capacitive humidity sensor compatible with CMOS technology," *Pan Tao Ti Hsueh Pao/Chinese J. Semicond.*, vol. 26, no. 7, pp. 1374–1378, 2005, [Online]. Available: https://www.scopus.com/inward/record.uri?eid=2-s2.0-23144458550&partnerID=40&md5=b27a91c623617c9862ce8b93b606d3e6

[23] M. Han, X. Ding, H. Duan, S. Luo, and G. Chen, "Ultrasensitive Humidity Sensors with Synergy between Superhydrophilic Porous Carbon Electrodes and Phosphorus-Doped Dielectric Electrolyte," *ACS Appl. Mater. Interfaces*, vol. 15, no. 7, pp. 9740–9750, 2023, doi: 10.1021/acsami.2c21051.

[24] C. Huang *et al.*, "Wide-detection-range, highly-sensitive, environmental-friendly and flexible cellulose-based capacitive humidity sensor," *Carbohydr. Polym.*, vol. 358, 2025, doi: 10.1016/j.carbpol.2025.123507.

[25] X. Yao and Y. Cui, "A PEDOT:PSS functionalized capacitive sensor for humidity," *Meas. J. Int. Meas. Confed.*, vol. 160, 2020, doi: 10.1016/j.measurement.2020.107782.

[26] Q. Ye, C. Wen, M. Xu, S.-L. Zhang, and D. Wu, "Ultra-sensitive and responsive capacitive humidity sensor based on graphene oxide," in *Proceedings - 2015 IEEE 11th International Conference on ASIC, ASICON 2015*, 2016. doi: 10.1109/ASICON.2015.7517015.

[27] Q. Wei *et al.*, "Design of a wireless skin moisture detection system using a capacitive sensor," in *Proceedings - IEEE-EMBS International Conference on Biomedical and Health Informatics: Global Grand Challenge of Health Informatics, BHI 2012*, 2012, pp. 261–264. doi: 10.1109/BHI.2012.6211561.

[28] V. Chaturvedi, M. Falk, S. Björklund, J. F. Gonzalez-Martinez, and S. Shleev, "Monoolein-Based Wireless Capacitive Sensor for Probing Skin Hydration," *Sensors*, vol. 24, no. 14, 2024, doi: 10.3390/s24144449.

[29] A. Lata, P. Maurya, and M. K. Singh, "Quality Assessment in Packaged Foods: Fringing Field Capacitive Sensors for Non-Invasive Moisture Content Detection and Beyond," in *2023 International Conference on Next Generation Electronics, NEleX 2023*, 2023. doi: 10.1109/NEleX59773.2023.10421689.

[30] M. A. Alsultan, J. Melia-Segui, J. Parron-Granados, and S. Lopez-Soriano, "A Battery-Less UHF RFID Sensor for Soil Moisture Monitoring," *IEEE J. Radio Freq. Identif.*, vol. 9, pp. 286–294, 2025, doi: 10.1109/JRFID.2025.3572843.

[31] C. Power, "A sense of purpose," *New Electron.*, vol. 39, no. 16, pp. 28–29, 2006, [Online]. Available: https://www.scopus.com/inward/record.uri?eid=2-s2.0-33750040862&partnerID=40&md5=d971106e38ec08b8a9da10bb2bc8be97

[32] G. Rigatos, M. Abbaszadeh, K. Busawon, L. Dala, J. Pomares, and F. Zouari, "Flatness-Based Control in Successive Loops for Autonomous Quadrotors," *J. Dyn. Syst. Meas. Control*, vol. 146, no. 2, p. 24501, 2024, doi: 10.1115/1.4063907.

[33] G. Rigatos, P. Siano, F. Zouari, and S. Ademi, "Nonlinear optimal control of autonomous submarines' diving," *Mar. Syst. Ocean Technol.*, vol. 15, no. 1, pp. 57–69, 2020, doi: 10.1007/s40868-019-00070-3.

[34] F. Zouari and M. Mahmud, "Neural Network-Based Robust Adaptive Output Feedback Control for MIMO Time-Varying Delay Systems," in *Applications of Artificial Intelligence and Data Science (AAIDS 2024)*, vol. 2601, M. Mahmud et al., Eds. Cham: Springer, 2026, pp. 60–77. doi: 10.1007/978-3-031-98498-3_5.

[35] G. Rigatos, P. Siano, F. Zouari, and S. Ademi, "A nonlinear optimal control method for autonomous submarines' diving," *2017 IEEE 26th International Symposium on Industrial Electronics (ISIE)*. IEEE, Edinburgh, United Kingdom, pp. 1061–1066. doi: 10.1109/ISIE.2017.8001393.

[36] A. Sofou, G. Evangelopoulos, and P. Maragos, "Soil image segmentation and texture analysis: A computer vision approach," *IEEE Geosci. Remote Sens. Lett.*, vol. 2, no. 4, pp. 394–398, 2005, doi: 10.1109/LGRS.2005.851752.

[37] E. M. Huerta, S. A. Z. Castro, and R. E. Ibanez Reguera, "Multiscale analysis by images of the microstructure of sandy sediments," in *2016 IEEE International Engineering Summit, IE-Summit 2016*, 2016. doi: 10.1109/IESummit.2016.7459770.

[38] A. Velmurugan and G. G. Carlos, "Soil resource assessment and mapping using remote sensing and GIS," *J. Indian Soc. Remote Sens.*, vol. 37, no. 3, pp. 511–525, 2009, doi: 10.1007/s12524-009-0045-3.

[39] A. DORNIK, L. DRĂGUŢ, and P. URDEA, "Classification of Soil Types Using Geographic Object-Based Image Analysis and Random Forests," *Pedosphere*, vol. 28, no. 6, pp. 913–925, 2018, doi: 10.1016/S1002-0160(17)60377-1.

[40] D. Kim, Y. Son, and J. Park, "Prediction of Settling Velocity of Nonspherical Soil Particles Using Digital Image Processing," *Adv. Civ. Eng.*, vol. 2018, 2018, doi: 10.1155/2018/4647675.

[41] E.-O. Babalola, M. H. Asad, and A. Bais, "Soil Surface Texture Classification Using RGB Images Acquired Under Uncontrolled Field Conditions," *IEEE Access*, vol. 11, pp. 67140–67155, 2023, doi: 10.1109/ACCESS.2023.3290907.

[42] A. Ramadhanu and R. A. Mahessya, "Development of Identification Methods Based on Soil Imagery Characteristics, Textures, and Shapes Suitable for Planting Food Crops," *Int. J. Intell. Syst. Appl. Eng.*, vol. 11, no. 3, pp. 825–832, 2023, [Online]. Available: https://www.scopus.com/inward/record.uri?eid=2-s2.0-85174854645&partnerID=40&md5=3f17f4d60095dce5a96cba6d030631d0

[43] T. Dawood, Z. Zhu, and T. Zayed, "Computer vision-based model for moisture marks detection and recognition in subway networks," *J. Comput. Civ. Eng.*, vol. 32, no. 4, p. 4018026, 2018, doi: 10.1061/(ASCE)CP.1943-5487.0000776.

[44] F. Greifeneder, C. Notarnicola, G. Bertoldi, and W. Wagner, "From point to pixel scale: An upscaling approach for in situ soil moisture measurements," *Vadose Zo. J.*, vol. 15, no. 9, pp. 1–8, 2016, doi: 10.2136/vzj2016.02.0012.

[45] G. Rigatos, M. Abbaszadeh, and F. Zouari, "Flatness-based control in successive loops for dual-arm robotic manipulators," *J. Vib. Control*, 2024, doi: 10.1177/10775463241286550.

[46] A. Boulkroune, A. Boubellouta, A. Bouzeriba, and F. Zouari, "Practical Finite-Time Fuzzy Synchronization of Chaotic Systems with Non-Integer Orders: Two Chattering-Free Approaches," *J. Syst. Sci. Syst. Eng.*, vol. 34, no. 3, pp. 334–359, 2025, doi: 10.1007/s11518-024-5635-7.